Aspect ratio effects on limited scrape-off layer plasma turbulence

Sébastien Jolliet, Federico D. Halpern, Joaquim Loizu, Annamaria Mosetto, and Paolo Ricci
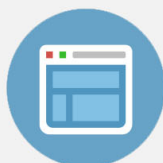
Aspect ratio effects on limited scrape-off layer plasma turbulence

Sébastien Jolliet,[a)] Federico D. Halpern, Joaquim Loizu, Annamaria Mosetto,
and Paolo Ricci

*École Polytechnique Fédérale de Lausanne (EPFL), Centre de Recherches en Physique des Plasmas,
Association Euratom-Confédération Suisse, CH-1015 Lausanne, Switzerland*

The drift-reduced Braginskii model describing turbulence in the tokamak scrape-off layer is written for a general magnetic configuration with a limiter. The equilibrium is then specified for a circular concentric magnetic geometry retaining aspect ratio effects. Simulations are then carried out with the help of the global, flux-driven fluid three-dimensional code GBS [Ricci *et al.*, Plasma Phys. Controlled Fusion **54**, 124047 (2012)]. Linearly, both simulations and simplified analytical models reveal a stabilization of ballooning modes. Nonlinearly, flux-driven nonlinear simulations give a pressure characteristic length whose trends are correctly captured by the gradient removal theory [Ricci and Rogers, Phys. Plasmas **20**, 010702 (2013)], that assumes the profile flattening from the linear modes as the saturation mechanism. More specifically, the linear stabilization of ballooning modes is reflected by a 15% increase in the steady-state pressure gradient obtained from GBS nonlinear simulations when going from an infinite to a realistic aspect ratio. © 2014 AIP Publishing LLC. [http://dx.doi.org/10.1063/1.4863956]

I. INTRODUCTION

The physical understanding of the scrape-off layer (SOL) is of crucial importance for determining the performance of future fusion devices such as ITER. This region, characterized by open field lines terminating on a limiter or on a divertor, exhausts the tokamak power, controls the plasma fueling and the impurity dynamics, affecting the overall plasma confinement.

In the SOL, the collision frequency is usually large, thus allowing to neglect off kinetic effects. It is therefore reasonable to use a fluid[1–3] or a gyro-fluid model[4,5] to describe the plasma dynamics in this regime. As the typical amplitude of fluctuations in the SOL is comparable to the background values, one needs a full-n model that does not separate between equilibrium and fluctuation quantities. Furthermore, since the characteristic length of the fluctuations in the SOL is comparable to the background one, a radially global approach is necessary. Then, a flux-driven model is preferred over a fixed-gradient model because the former is closer to experimental conditions, where profiles result from a balance between sources and losses and are *a-priori* unknown, exhibiting richer physics such as the appearance of avalanches[6] and self-consistent interactions between the background and the fluctuations. Such fluid flux-driven simulations have emerged,[6–9] allowing to simulate SOL plasma turbulence and shedding light on the crucial physical phenomena at play in this region. In a recent publication,[10] it has been shown that the gradient-removal theory is able to predict relatively well the sustainable pressure gradient inside the SOL for 3D fluid simulations in limited geometry. The validity of this theory has been further confirmed in a large number of turbulent electrostatic regimes[11] as well as in electromagnetic simulations.[12]

Although the importance of including a realistic magnetic equilibrium to study turbulence has been known since the early 1980s,[13] only a small number of studies have been carried out in the SOL with an advanced geometry. The mirror force has been found to play an important role in the SOL of MAST,[14,15] while the aspect ratio dependence of the parallel flow profile in the SOL has been investigated in a 2D particle code.[16] Aspect ratio effects are thought to play an important role in determining the characteristic cross-sectional area of the SOL and explain in part the improvement of confinement when moving the toroidal limiter from the low-field-side to the high-field-side of the tokamak.[17] In the plasma edge, a reduction of transport due to elongation is observed in gyrofluid turbulence,[18] while some aspect ratio effects in collisional drift wave turbulence are briefly discussed in Ref. 19. Magnetic shaping also affects the edge propagation of geodesic acoustic modes, which extract the zonal flows energy, thus enhancing turbulence levels.[20,21]

While some codes have the capability to treat arbitrary magnetic shapes, most of the studies focus on comparisons with experiments (through the coupling of a turbulence code with an equilibrium solver) rather than studying the specific effects of shaping on turbulence. The aim of this work is to study aspect ratio effects on SOL fluid turbulence. First, the drift-reduced Braginskii equations used to evolve the SOL plasma dynamics are derived in arbitrary magnetic geometry. A magnetic equilibrium with circular flux surfaces retaining finite aspect ratio effects[22] is then prescribed. The effects of this particular geometry are studied on the growth of linear modes and, by using the 3D global fluid code GBS[7] and the gradient removal theory, a detailed analysis of nonlinear simulations including finite aspect ratios is carried out. In particular, aspect ratio effects are introduced in a simple linear dispersion relation describing the most basic features of resistive ballooning modes (RBMs). This analytical model is able to predict the behaviour of linear modes in the system.

a)Electronic mail: sebastien.jolliet@epfl.ch

It is also demonstrated in this paper that, through the comparison with nonlinear simulations, the gradient removal theory is able, using only a linear dispersion relation, to predict aspect ratio effects on the nonlinearly sustained pressure gradient. Therefore, the main result of this work is an analytical method to predict aspect ratio effects on the SOL width: By decreasing the amplitude of the curvature at the low field side of the tokamak with respect to the infinite aspect ratio case, aspect ratio effects reduce the linear growth of ballooning modes. This in turns leads to a decrease of the SOL width.

The paper is organized as follows. In Sec. II, the drift-reduced Braginskii equations are derived in a general axisymmetric magnetic field configuration. The magnetic geometry studied in this work allows to pinpoint finite aspect ratio effects and is detailed in Sec. III. In Sec. IV, the impact of aspect ratio effects on the linear growth rate of the SOL unstable modes is studied. Nonlinear simulations using the GBS code[10] are then presented in Sec. V and results are compared with predictions of the gradient removal theory. Finally, conclusions are drawn in Sec. VI.

II. FLUID MODEL IN THE SOL

A. Fluid moment equations

The study of the SOL presented in this paper is based on the two-fluid, electrostatic, cold ion ($T_i = 0$) drift-reduced Braginskii equations. By assuming that the orderings $\mathrm{d}/\mathrm{d}t \ll \omega_{ci}$ ($\omega_{ci} = eB/m_i$ is the ion gyrofrequency) and $k_\perp \gg k_\parallel$ hold over the whole domain, the perpendicular velocities are written as $\mathbf{V}_{\perp i} = \mathbf{V}_{E\times B} + \mathbf{V}_{pol}$ and $\mathbf{V}_{\perp e} = \mathbf{V}_{E\times B} + \mathbf{V}_{*e}$, where $\mathbf{V}_{E\times B} = (-\nabla\phi \times \mathbf{B})/B^2$ is the $E\times B$ drift velocity, $V_{*e} = -(1/enB^2)\mathbf{B} \times \nabla p_e$ is the electron diamagnetic drift, e is the elementary charge, and $\mathbf{V}_{pol}$ is the polarization velocity defined in Ref. 3. The continuity, vorticity, ion, and electron parallel momentum and electron temperature equations then read, in normalized form

$$\partial_t n = -\frac{R_0}{B}[\phi, n] - \nabla_\parallel(nv_{\parallel e}) - nv_{\parallel e}\nabla \cdot \mathbf{b}$$
$$+ \frac{2}{B}[C(p_e) - nC(\phi)] + S_n + D_n\nabla_\perp^2 n \quad (1)$$

$$\partial_t \omega = -\frac{R_0}{B}[\phi, \omega] - v_{\parallel i}\nabla_\parallel\omega + \frac{2B}{n}C(p_e)$$
$$+ B^2\left[\frac{1}{n}\nabla_\parallel j_\parallel + \frac{j_\parallel}{n}\nabla \cdot \mathbf{b}\right]$$
$$+ \frac{B}{3n}C(G_i) + D_\omega\nabla_\perp^2\omega \quad (2)$$

$$\partial_t v_{\parallel e} = -\frac{R_0}{B}[\phi, v_{\parallel e}] - v_{\parallel e}\nabla_\parallel v_{\parallel e} + D_{v_{\parallel e}}\nabla_\perp^2 v_{\parallel e},$$
$$+ \frac{m_i}{m_e}\left\{\nu\frac{j_\parallel}{n} + \nabla_\parallel\phi - \frac{1}{n}\nabla_\parallel p_e - 0.71\nabla_\parallel T_e - \frac{2}{3n}\nabla_\parallel G_e\right\} \quad (3)$$

$$\partial_t v_{\parallel i} = -\frac{R_0}{B}[\phi, v_{\parallel i}] - v_{\parallel i}\nabla_\parallel v_{\parallel i} - \frac{1}{n}\nabla_\parallel p_e - \frac{2}{3n}\nabla_\parallel G_i$$
$$+ D_{v_{\parallel i}}\nabla_\perp^2 v_{\parallel i}, \quad (4)$$

$$\partial_t T_e = -\frac{R_0}{B}[\phi, T_e] - v_{\parallel e}\nabla_\parallel T_e$$
$$+ \frac{4}{3B}T_e\left[\frac{7}{2}C(T_e) + \frac{T_e}{n}C(n) - C(\phi)\right] + S_{T_e}$$
$$+ \frac{2}{3}T_e\left[0.71\nabla_\parallel v_{\parallel i} - 1.71\nabla_\parallel v_{\parallel e} + 0.71\left(\frac{v_{\parallel i} - v_{\parallel e}}{n}\right)\nabla_\parallel n\right]$$
$$+ T_e(0.71v_{\parallel e} - 1.71v_{\parallel i})\nabla \cdot \mathbf{b} + D_{T_e}\nabla_\perp^2 T_e + \chi_\parallel\nabla_\parallel^2 T_e, \quad (5)$$

where R_0 is the tokamak major radius expressed in ρ_{s0} units, $\omega = \nabla_\perp^2\phi$ is the vorticity, $j_\parallel = n(v_{\parallel i} - v_{\parallel e})$ is the parallel current, $\mathbf{b} = \mathbf{B}/B$ is the unit magnetic field vector, ν is the normalized Spitzer resistivity, and $\chi_\parallel$ is the parallel heat flux diffusivity given as an input constant. Quasineutrality is assumed such that $n_e = n_i \equiv n$. Plasma outflow from the closed flux surface region is mimicked using density and temperature sources, respectively, S_n and S_{T_e}. The G_e and G_i terms represent the gyroviscous part of the pressure tensor and are given by

$$G_i = -3\eta_{0i}\left[\frac{2}{3}\nabla_\parallel v_{\parallel i} + \frac{1}{3B}C(\phi)\right], \quad (6)$$

$$G_e = -3\eta_{0e}\left[\frac{2}{3}\nabla_\parallel v_{\parallel e} + \frac{1}{3B}C(\phi) - \frac{1}{3Bn}C(p_e)\right], \quad (7)$$

where η_{0i} and η_{0e} are constant coefficients given on input. Furthermore, the vorticity equation has been obtained using the common Boussinesq approximation

$$\nabla \cdot \left(\frac{nm_i}{B^2 e}\frac{\mathrm{d}}{\mathrm{d}t}\nabla_\perp\phi\right) \cong \frac{nm_i}{B^2 e}\frac{\mathrm{d}}{\mathrm{d}t}\nabla_\perp^2\phi. \quad (8)$$

Small perpendicular diffusion terms of the form $D_a\nabla_\perp^2 a$ are added for numerical reasons. Perpendicular laplacians are assumed to lie in the poloidal plane (see Appendix A). The curvature operator is defined by $C(A) = B/2$ $[\nabla \times (\mathbf{b}/B)] \cdot \nabla A$, the parallel gradient is $\nabla_\parallel A = \mathbf{b} \cdot \nabla A$, the perpendicular laplacian is $\nabla_\perp^2 A = -\nabla \cdot [\mathbf{b} \times (\mathbf{b} \times \nabla A)]$ and the Poisson bracket is $[\phi, A] = \mathbf{b} \cdot (\nabla\phi \times \nabla A)$. The normalizations are (tilde denotes quantities in physical units): $t = \tilde{t}/(R_0/c_{s0})$, $\nabla_\perp = \tilde{\nabla}_\perp\rho_{s0}$, $\nabla_\parallel = \tilde{\nabla}_\parallel R_0$, $v = \tilde{v}/c_{s0}$, $n = \tilde{n}/n_0$, $T_e = \tilde{T}_e/T_{e0}$, $\phi = e\tilde{\phi}/T_{e0}$, $\nu = \tilde{\nu}/(c_{s0}m_e/R_0 m_i)$, with $c_{s0} = \sqrt{T_{e0}/m_i}$ and $\rho_{s0} = c_{s0}/\omega_{ci}$ where ω_{ci} is evaluated with the magnetic field at the magnetic axis, while T_{e0} and n_0 are the reference temperature and density.

The above system of equations is implemented with a proper set of boundary conditions to describe the interface between the SOL and the magnetic pre-sheath where the ion drift approximation $\mathrm{d}/\mathrm{d}t \ll \omega_{ci}$ breaks down.[23] At the top and at the bottom of the limiter, these are, in normalized units, $v_{\parallel i} = \pm\sqrt{T_e}$, $v_{\parallel e} = \pm\sqrt{T_e}\exp(\Lambda - \phi/T_e)$, $\partial_s n = \mp n/\sqrt{T_e}\partial_s v_{\parallel i}$, $\partial_s\phi = \mp\sqrt{T_e}\partial_s v_{\parallel i}$, $\omega = -(\partial_s v_{\parallel i})^2 \mp \sqrt{T_e}\partial_{ss}v_{\parallel i}$ and $\partial_s T_e = \kappa_T/T_e\partial_s\phi$, with $\Lambda = 3$ and $\kappa_T = 0.15$. Here, s is a coordinate normal to the limiter walls. Corrections of order ρ_{s0}/L_p described in Ref. 23 have been neglected.

B. Magnetic field dependence in the fluid model

The system of equations presented in this paper considers, with respect to the system of equations presented in Ref. 7, an arbitrary magnetic field configuration. The modulus of the magnetic field B, the divergence of the unitary magnetic field vector $\nabla \cdot \mathbf{b}$, the differential operators $\nabla_\parallel$, $\nabla_\perp^2$ as well as the curvature operator C and the Poisson bracket operator $[\phi, A]$ depend on the particular form of the magnetic field vector $\mathbf{B}$. The magnetic field configuration enters therefore in Eqs. (1)–(5) through six operators

$$[\phi, A] = \frac{1}{\mathcal{J}} \epsilon_{ijk} b_i \frac{\partial \phi}{\partial \xi^j} \frac{\partial A}{\partial \xi^k}, \tag{9}$$

$$\nabla_\parallel A = b^j \frac{\partial A}{\partial \xi^j}, \tag{10}$$

$$C(A) = \frac{B}{2\mathcal{J}} \frac{\partial c_m}{\partial \xi^j} \frac{\partial A}{\partial \xi^k} \epsilon_{kjm}, \tag{11}$$

$$\nabla_\perp^2 A = \frac{1}{\mathcal{J}} \frac{\partial}{\partial \xi^k} \left(\mathcal{J}^{-1} \epsilon_{klm} \epsilon_{i\alpha\beta} g_{mi} b_l b_\alpha \frac{\partial A}{\partial \xi^\beta} \right), \tag{12}$$

$$\nabla \cdot \mathbf{b} = \frac{1}{\mathcal{J}} \frac{\partial}{\partial \xi^i} (b^i \mathcal{J}), \tag{13}$$

$$B = \sqrt{B^j B_j}, \tag{14}$$

where the Einstein summation convention is assumed, ϵ_{ijk} is the Levi-Civita tensor, $\{\xi^i\} = \{\xi^1, \xi^2, \xi^3\}$ is an arbitrary set of coordinates, $\mathbf{b} = \mathbf{B}/B$, $c_m = b_m/B$, $g^{ij} = \nabla \xi^i \cdot \nabla \xi^j$ is the contravariant metric tensor, $g_{ij} = \text{Inv}(g^{ij})$ is the covariant metric tensor, and $\mathcal{J} = 1/\sqrt{\det(g^{ij})}$ is the Jacobian, $b^i = \mathbf{b} \cdot \nabla \xi^i$, $b_i = g_{ij} b^j$. These operators can be computed by knowing the covariant and contravariant coordinates of the magnetic field and the metric tensor for any coordinate system.

The general axisymmetric form for the magnetic field is considered in this study

$$\mathbf{B} = F(\psi) \nabla \varphi + \nabla \psi \times \nabla \varphi, \tag{15}$$

where ψ is the poloidal flux function, which is in general a solution of the Grad-Shafranov equation, $F(\psi)$ describes the toroidal magnetic field and φ is the toroidal angle.

C. Coordinate systems

Turbulence is often represented in the toric coordinate system $(x = r, y = a\theta_*, z = R_0 \varphi)$, where r is a flux coordinate, a is the tokamak minor radius, and the straight-field-line angle θ_* is defined as

$$\theta_* = \frac{1}{q(r)} \int_0^\theta d\theta' \frac{\mathbf{B} \cdot \nabla \varphi}{\mathbf{B} \cdot \nabla \theta'}. \tag{16}$$

θ is a poloidal coordinate and $q(r)$ is the safety factor

$$q(r) = \frac{1}{2\pi} \int_0^{2\pi} d\theta \frac{\mathbf{B} \cdot \nabla \varphi}{\mathbf{B} \cdot \nabla \theta}. \tag{17}$$

The straight-field-line angle is such that $\mathbf{B} \cdot \nabla \theta_* = q(r) \mathbf{B} \cdot \nabla \varphi$. In other words, magnetic field lines are straight in the (θ_*, φ) plane. A model implementation in the (x,y,z) coordinate system is usually simple but the parallel dynamics must be treated carefully as the grid is not aligned with magnetic field lines.

In order to take advantage of the strong anisotropy of turbulence, it is computationally efficient to use coordinates that are aligned with the magnetic field. One can define a field-line label $\alpha = \varphi - q(r) \theta_*$, from which the flux-tube coordinates $X = r, Y = (a/q_0)\alpha, Z = q_0 R_0 \theta_*$ are derived, with $q_0 \equiv q(a)$ a reference safety factor. The (X,Y) plane is perpendicular to the magnetic field, and Z becomes a field-aligned coordinate. Due to long parallel wavelengths, turbulent simulations can be performed at low Z resolution which strongly reduces the computational time. However, the non-periodicity of the α coordinate requires some complicated treatment in global geometry for the boundary conditions.[24] Operators (9)–(12) can be written in advection form

$$[\phi, A] = \mathcal{P}_{XY}[\phi, A]_{XY} + \mathcal{P}_{YZ}[\phi, A]_{YZ} + \mathcal{P}_{ZX}[\phi, A]_{ZX}, \tag{18}$$

$$\nabla_\parallel A = \mathcal{D}^X \frac{\partial A}{\partial X} + \mathcal{D}^Y \frac{\partial A}{\partial Y} + \mathcal{D}^Z \frac{\partial A}{\partial Z}, \tag{19}$$

$$C(A) = \mathcal{C}^X \frac{\partial A}{\partial X} + \mathcal{C}^Y \frac{\partial A}{\partial Y} + \mathcal{C}^Z \frac{\partial A}{\partial Z}, \tag{20}$$

$$\begin{aligned}\nabla_\perp^2 A &= \mathcal{N}^{XX} \frac{\partial^2 A}{\partial X^2} + \mathcal{N}^{XY} \frac{\partial^2 A}{\partial X \partial Y} + \mathcal{N}^{YY} \frac{\partial^2 A}{\partial Y^2} + \mathcal{N}^X \frac{\partial A}{\partial X} + \mathcal{N}^Y \frac{\partial A}{\partial Y} \\ &+ \mathcal{N}^{ZZ} \frac{\partial^2 A}{\partial Z^2} + \mathcal{N}^{XZ} \frac{\partial^2 A}{\partial X \partial Z} + \mathcal{N}^{YZ} \frac{\partial^2 A}{\partial Y \partial Z} + \mathcal{N}^Z \frac{\partial A}{\partial Z},\end{aligned} \tag{21}$$

where $[\phi, A]_{XY} = \partial A/\partial X \partial \phi/\partial Y - \partial A/\partial Y \partial \phi/\partial X$. Equivalent expressions are found with the coordinate system (x,y,z). Note that the above relations are global and only assume the axisymmetry of the magnetic field. Each coefficient is therefore a function of x and y. The detailed expressions of the operators are derived in Appendix A. All the magnetic equilibrium information is contained in these coefficients. In practice, implementing a new magnetic configuration is equivalent to finding the expression (whether analytical or numerical) of these coefficients. An example is given in Sec. III.

III. CIRCULAR MAGNETIC FLUX SURFACES WITH ASPECT RATIO EFFECTS

In the present paper, a magnetic equilibrium with circular magnetic surfaces, retaining finite aspect ratio effects is considered. The local inverse aspect ratio, noted ϵ, is defined as $\epsilon = r/R_0$, where R_0 is the major radius of the tokamak. The magnetic field is completely defined by setting $F(\psi) = B_0 R_0$ and the shape of magnetic surfaces

$$R_c = R_0 + r \cos \theta, \tag{22}$$

$$Z_c = r \sin \theta, \tag{23}$$

where (R_c, Z_c) are standard cylindrical coordinates in the poloidal plane. The poloidal flux $\psi \equiv \psi(r)$ can be expressed

as a function of the safety factor through Eq. (17), giving $\psi'(r) = B_0 r / \bar{q}(r)$, where $\bar{q}$ is a pseudo safety factor such that $q(r) = \bar{q}(r)/\sqrt{1-\epsilon^2}$. In this geometry, the (r, θ) coordinates coincide with the usual polar coordinates. The straight-field-line can be analytically computed from Eq. (16)

$$\theta_* = 2 \tan^{-1}\left[\sqrt{\frac{1-\epsilon}{1+\epsilon}} \tan(\theta/2)\right], \qquad (24)$$

from which it is trivial to see that $\lim_{\epsilon \to 0} \theta_* = \theta$. A circular, concentric model is a solution of the Grad-Shafranov equation if the latter is expanded up to first order in ϵ at $\beta = 0$ and the Shafranov shift is negligible. This model is therefore not appropriate for low aspect ratio tokamaks $R_0/a \lesssim 3$. Mathematically, this is expressed by the fact that θ_* is not defined for $\epsilon \to 1$ as can be seen in Eq. (24).

In practice, implementing an equilibrium means computing the metric tensor and the magnetic field components associated with the chosen coordinate system. First, the covariant metric tensor in (θ, r, φ) coordinates is obtained from Eqs. (22)–(23), for example, $g_{rr} = (\partial R_c/\partial r)^2 + (\partial Z_c/\partial \theta)^2$. The contravariant metric tensor in (θ, r, φ) coordinates is then obtained by inverting the covariant one. The contravariant metric tensor coefficients for (θ_*, r, φ) are then given by

$$g^{\theta_* \theta_*} = \left(\frac{\partial \theta_*}{\partial \theta}\right)^2 g^{\theta\theta} + 2\frac{\partial \theta_*}{\partial \theta}\frac{\partial \theta_*}{\partial r} g^{r\theta} + \left(\frac{1}{R_0}\frac{\partial \theta_*}{\partial \epsilon}\right)^2 g^{rr},$$

$$g^{\varphi\varphi} = \frac{1}{R_c^2}, \qquad (25)$$

$$g^{\theta_* r} = \frac{\partial \theta_*}{\partial \theta} g^{r\theta} + \frac{1}{R_0}\frac{\partial \theta_*}{\partial \epsilon} g^{rr}, \quad g^{r\varphi} = g^{\theta_* \varphi} = 0, \qquad (26)$$

$$g^{\theta_* \alpha} = -\hat{s}\theta_* \frac{q}{r} g^{\theta_* r} - q g^{\theta_* \theta_*}, \qquad (27)$$

$$g^{r\alpha} = -\hat{s}\theta_* \frac{q}{r} g^{rr} - q g^{\theta_* r}, \qquad (28)$$

$$g^{\alpha\alpha} = g^{\varphi\varphi} + q^2 g^{\theta_* \theta_*} + 2\frac{q^2 \hat{s}\theta_*}{r} g^{\theta_* r} + (\hat{s}\theta_*)^2 \frac{q^2}{r^2} g^{rr}, \qquad (29)$$

where $\hat{s} = r q'(r)/q(r)$ is the magnetic shear,

$$\frac{\partial \theta_*}{\partial \theta} = \frac{1 - \epsilon \cos\theta_*}{\sqrt{1-\epsilon^2}}, \qquad (30)$$

$$\frac{\partial \theta_*}{\partial \epsilon} = -\frac{\sin\theta_*}{1-\epsilon^2}, \qquad (31)$$

$$R_c = R_0 \frac{1-\epsilon^2}{1-\epsilon\cos\theta_*}, \qquad (32)$$

and the Jacobian associated with the metric tensor is

$$\mathcal{J} = 1/\sqrt{\det(g^{ij})} = R_0 r \frac{(1-\epsilon^2)^{3/2}}{(1-\epsilon\cos\theta_*)^2}. \qquad (33)$$

The covariant metric tensor can be easily calculated as a function of the contravariant one, for example, $g_{rr} = \mathcal{J}^2 (\nabla\alpha \times \nabla\theta_*) \cdot (\nabla\alpha \times \nabla\theta_*) = \mathcal{J}^2 (g^{\theta_*\theta_*} g^{\alpha\alpha} - g^{\theta_*\alpha} g^{\theta_*\alpha})$.

The contravariant component of the magnetic field for a coordinate ξ_i is given by $B^i = \mathbf{B} \cdot \nabla\xi_i$ and the associated covariant component is given by $B_i = g_{ij} B^j$. For the present geometry, $B^\varphi = (B_0 R_0)/R_c^2$ and $B^{\theta_*} = \psi'/\mathcal{J}$. Using the covariant and contravariant components of the metric tensor and the magnetic field as well as the derivatives of these coefficients, the coefficients in the operators (18) to (21) can be analytically obtained. Their detailed expressions are given in Appendix B for both toric and flux tube coordinate systems.

The model used in earlier studies of the SOL[7,12,23,25] adopted the usual $s - \alpha$ geometry[26] which describes circular concentric surfaces in the large aspect ratio limit $\epsilon \to 0$. In this model, the modulus of the magnetic field, B, is assumed constant and the straight-field-line angle is approximated to the poloidal angle θ, where $q(r)$ is the safety factor. It is shown in Appendix C that the model considered here and the $s - \alpha$ models are equivalent in the $\epsilon \to 0$ limit.

In the remaining of the paper, the equilibrium will be approximated to be local in the radial direction. In particular, the inverse aspect ratio ϵ is evaluated at the last closed surface, i.e., $\epsilon = a/R_0$ and the safety factor is constant throughout the simulation domain.

IV. LINEAR ASPECT RATIO EFFECTS

The influence of finite aspect ratio effects on the growth of linear unstable modes is now investigated. To this aim, the drift-reduced Braginksii equations (1) to (5) are linearized, assuming an equilibrium density and temperature profile dependent on the radial coordinate only. Each physical quantity A is therefore split according to $A = A_0(X) + \delta A(Y, Z)$, where A_0 is a local radial equilibrium at $r = a$ and δA is the perturbation. The equilibrium gradient is defined by $\partial A_0/\partial X \to -A_0/L_A$, where L_A is the characteristic length of the field A. By setting $\phi_0 = v_{\|e0} = v_{\|i0} = 0$, the plasma equilibrium is defined through a density and temperature gradient. The linearised drift-reduced Braginskii equations are

$$\frac{\partial \delta n}{\partial t} = \frac{R_0}{L_n}\frac{1}{B}\mathcal{P}^L(\delta\phi) + \frac{2}{B}C^L(\delta n - \delta\phi + \delta T_e) - (\nabla_\| + \nabla \cdot \mathbf{b})\delta v_{\|e}, \qquad (34)$$

$$\frac{1}{B^2}(\nabla_\perp^2)^L \frac{\partial \delta\phi}{\partial t} = \frac{2}{B}C^L(\delta n + \delta T_e) + (\nabla_\| + \nabla \cdot \mathbf{b})(\delta v_{\|i} - \delta v_{\|e}), \qquad (35)$$

$$\frac{m_e}{m_i}\frac{\partial \delta v_{\|e}}{\partial t} = \nabla_\|(\delta\phi - \delta n) - 1.71\nabla_\|\delta T_e + \frac{m_e}{m_i}\nu(\delta v_{\|e} - \delta v_{\|i}), \qquad (36)$$

$$\frac{\partial \delta T_e}{\partial t} = \frac{R_0}{L_n}\eta\frac{1}{B}\mathcal{P}^L(\delta\phi) + \frac{4}{3B}C^L(\delta n - \delta\phi + 7/2\delta T_e) + \frac{2}{3}(\nabla_\| + \nabla \cdot \mathbf{b})(0.71\delta v_{\|i} - 1.71\delta v_{\|e}), \qquad (37)$$

$$\frac{\partial \delta v_{\|i}}{\partial t} = -\nabla_\|(\delta n + \delta T_e), \qquad (38)$$

where $\eta = L_n/L_{Te}$, $\mathcal{P}^L$, $(\nabla_\perp^2)^L$ and C^L are the linearized expressions of the Poisson bracket, the perpendicular

laplacian and the curvature operator. In flux-tube geometry, they read

$$\mathcal{P}^L(A) = \mathcal{P}_{XY}\frac{\partial A}{\partial Y} + \mathcal{P}_{YZ}\frac{\partial A}{\partial Z}, \tag{39}$$

$$C^L(A) = \mathcal{C}^Y\frac{\partial A}{\partial Y} + \mathcal{C}^Z\frac{\partial A}{\partial Z}, \tag{40}$$

$$(\nabla_\perp^2)^L A = \mathcal{N}^{YY}\frac{\partial^2 A}{\partial Y^2} + \mathcal{N}^Y\frac{\partial A}{\partial Y}. \tag{41}$$

It has been checked analytically and numerically that $\mathcal{P}_{YZ}$, $\mathcal{C}^Z$ and $\mathcal{N}^Y$ are small and can be neglected.

In order to study the growth of linear modes in a limited SOL configuration, a numerical code, described in Ref. 25, has been developed. Perturbations are imposed to have the form $\delta A(Z)\exp[i(k_Y Y + \gamma t)]$ and the Z coordinate is discretized using 4th order centered finite differences. Dirichlet boundary conditions are applied for the perturbed potential, density, and temperature, while no boundary conditions are imposed for the ion and electron velocities. Various types of boundary conditions have been tested for ballooning modes and drift waves and no significant impact on the growth rate was found. Note that this contrasts with global modes such as ideal ballooning modes for which the boundary conditions are important.[12] The Z (resp. Y) coordinate is normalized to R_0 (resp. ρ_{s0}). The resulting linear system is integrated implicitly in time, and the growth rate γ is extracted as a function of the phase space parameters $(R_0/L_n, \eta, \nu, q, \epsilon, k_Y)$.

The linearized equations (34)–(38) are able to describe inertial and resistive drift wave modes, due to the $E \times B$ convection in the presence of non-adiabatic electrons, as well as inertial and resistive ballooning modes, driven unstable by the unfavorable curvature in the low-field side region. A thorough linear study of these linear instabilities can be found in Ref. 25 and, in Ref. 11, it is shown that RBMs dominate for typical limited SOL parameters. In the following, a set of parameters representative of this instability is considered. Parameters are $\eta = 1$, $q = 4$, $\hat{s} = 0$, $\nu = 0.1$, and $R_0/L_n = 10$. In essence, RBM eigenfunctions have a bell shape peaking around $\theta_* = 0$ in the parallel direction with $k_\parallel \rightarrow 1/(qR_0)$. Also, artificially removing the curvature operator leads to a strong decrease of the growth rate.

Note that magnetic equilibrium effects influence the linear dynamics through four distinct mechanisms: the $E \times B$ convection expressed by the $(1/B)[\phi, A]$ operator, the parallel convection, described by the $\nabla_\parallel + \nabla \cdot \mathbf{b}$ operator, the $(1/B)\,C(A)$ operator, and finally the vorticity operator expressed by $(1/B^2)\nabla_\perp^2$. Aspect ratio effects may be studied by introducing ϵ corrections, one by one, inside these different operators in the linearized Braginskii equations while keeping all the other parameters fixed. A scan in (k_Y, ϵ) is performed and the maximum growth rate over k_Y is selected for each value of ϵ. It is observed that the peak growth rate shifts from $k_y = 0.62$ to $k_y = 0.89$ for $\epsilon = 0$ and $\epsilon = 0.25$, respectively. However, it is noted that the growth rate is fairly flat around its peak in k_y. Results are summarized in Fig. 1. Introducing ϵ effects in the parallel gradient enhances the growth rate while the opposite effect is seen in the $(1/B)\,C(A)$ operator. The presence of aspect ratio effects in the Poisson brackets and the vorticity operator does not affect the growth rate significantly. Overall, when all aspect ratio effects are included, the growth rate is reduced by 20% at $\epsilon = 0.25$. The qualitative behavior of each curve can be explained by looking at a simple analytical dispersion relation describing the main features of RBMs[12]

$$\frac{\partial \delta p}{\partial t} = \frac{R_0}{L_p}\frac{1}{B}\mathcal{P}^L(\delta\phi), \tag{42}$$

$$\frac{1}{B^2}\frac{\partial \nabla_\perp^2 \delta\phi}{\partial t} = \frac{2}{B}C^L(\delta p) + \nabla_\parallel \delta j_\parallel, \tag{43}$$

$$0 = \nu\delta j_\parallel + \nabla_\parallel \delta\phi. \tag{44}$$

The dispersion relation is obtained by setting $\partial/\partial Y \rightarrow ik_Y$, $\partial/\partial t \rightarrow \gamma$, $\nabla_\parallel \rightarrow ik_\parallel$, keeping the leading term in ϵ, and assuming a strongly ballooned mode around $\theta_* = 0$. This allows to expand the differential operators

$$\frac{1}{B}\mathcal{P}^L(A) \cong -\frac{R_0}{L_n}\left(1 - \frac{1}{2}\epsilon^2\right)\frac{\partial A}{\partial Y} \rightarrow \frac{R_0}{L_p}\left(1 - \frac{\epsilon^2}{2}\right)ik_Y, \tag{45}$$

$$\nabla_\parallel A \cong (1 - \epsilon\cos\theta_*)\frac{\partial A}{\partial Z} \rightarrow (1 - \epsilon)ik_\parallel, \tag{46}$$
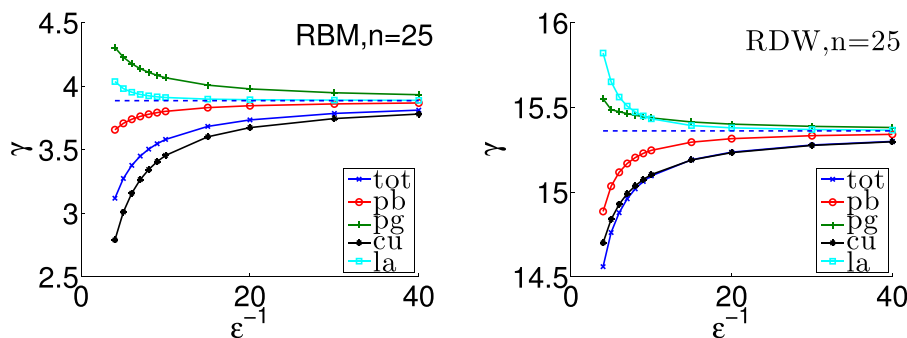

FIG. 1. Growth rate as a function of the aspect ratio for a Resistive Ballooning Mode (left) and a Resistive Drift Wave (right). The value of k_Y maximising the growth rate is chosen for each ϵ. Aspect ratio are turned on individually in the Poisson Bracket operator (red, circles), the parallel gradient and $\nabla \cdot \mathbf{b}$ operators (green, pluses), the $(1/B)C(A)$ operator (black, stars), and the vorticity operator $(1/B^2)\nabla_\perp^2$ (cyan, squares). The blue curve (crosses) shows the full aspect ratio corrections

$$\frac{1}{B} C^L(A) \cong -[\cos\theta_* - \epsilon(2 - \cos^2\theta_*)]\frac{\partial A}{\partial Y} \to -[1-\epsilon]ik_Y, \tag{47}$$

$$\frac{1}{B^2}(\nabla_\perp^2)^L A \cong (1 - \epsilon^2\cos^2\theta_*)\frac{\partial^2 A}{\partial Y^2} \to -(1-\epsilon^2)k_Y^2. \tag{48}$$

It has been checked that the scalar $\nabla \cdot \mathbf{b}$ does not influence linear growth rates significantly. The dispersion relation then writes

$$0 = \gamma^2 + 2\gamma_D\gamma - \gamma_I^2, \tag{49}$$

$$\gamma_D = \frac{k_\parallel^2(1-\epsilon)^2}{2k_Y^2(1-\epsilon^2)\nu}, \tag{50}$$

$$\gamma_I = \frac{1}{(1-\epsilon^2/2)}\sqrt{\frac{2R_0}{L_p}(1-\epsilon)(1-\epsilon^2/2)}. \tag{51}$$

In the large resistivity limit, the instability is a pure interchange mode with a growth rate $\gamma = \gamma_I$, resulting from the combination of the pressure gradient drive and the magnetic curvature operator. Finite $k_\parallel$ effects introduce a damping on the mode through the γ_D coefficients. In the following analysis, the value of k_Y will be kept constant, independent of ϵ. This assumption is appropriate since, in the linear simulations of the "full" system presented above, the growth rate is very weakly dependent on k_Y close to its peak.

From Eq. (45), aspect ratio effects on the $E \times B$ convection operator will decrease the drive by a small factor $\sqrt{(1-\epsilon^2/2)}$. The parallel damping term γ_D will be decreased by a factor $(1-\epsilon)^2 \cong (1-2\epsilon)$ according to Eq. (46) and this should result in a higher growth rate. Finite aspect ratio effects in the $(1/B)\,C(A)$ operator should decrease the growth rate as $\gamma_I \cong \sqrt{2(1-\epsilon)R_0/L_p}$. Finally, the vorticity operator should slightly increase γ_I by a factor $1/(1-\epsilon^2/2)$ and γ_D by a factor $1/(1-\epsilon^2)$, leading in a slight increase of the growth rate γ. All these dependences are qualitatively reproduced in Fig. 1. ϵ effects can be described as a balance between a decreased parallel damping and a reduced curvature drive, while other effects are of higher order in ϵ. Simulations show that this behavior is independent of the toroidal mode number. Remark that a similar reduction of the curvature operator $|C(A)| = |C_{\epsilon=0}(A) - \epsilon|$ has been obtained in Ref. 27.

The right panel of Fig. 1 displays the same analysis for a density gradient value of $R_0/L_n = 70$. In this case, the growth rate peak shifts from $k_y = 0.62$ to $k_y = 0.57$ when going from $\epsilon = 0$ to $\epsilon = 0.25$, respectively. At this density gradient value the fastest linear instability in the system is linearly unstable for resistive drift waves (RDW). Results are qualitatively similar, however the quantitative change of about 5% in the growth rate for $\epsilon = 1/4$ is much smaller compared to the RBM case. This is because the curvature plays a minor role in setting the amplitude of the instability. The eigenfunctions exhibit a finite $k_\parallel$ and extend over the whole θ_* domain. As a matter of fact, an analytical estimate of aspect ratio effects is more difficult to obtain than in the RBM case. In particular, aspect ratio effects on the parallel gradient

operator seem to have a very small impact on the growth rate. Similarly to the RBM case, the second order ϵ effects in the Poisson bracket and vorticity operators do not affect the growth rate significantly.

V. ASPECT RATIO EFFECTS ON NON-LINEAR SIMULATIONS

A. Implementation and simulation setup

The circular flux surface geometry with aspect ratio effects described in Sec. III has been implemented in the GBS code, initially developed to perform simulations in basic plasma physics devices[28–31] and then ported to the $s - \alpha$ tokamak geometry.[26] GBS results have been validated against experimental data from the TORPEX device.[32–34]

The main properties of the GBS code are briefly summarized here for completeness. More details can be found in Ref. 7. The toric coordinate system ($x = r, y = a\theta_*, z = R_0\varphi$) is employed and all the magnetic field quantities, including the safety factor, are radially local. Eqs. (1) to (5) are integrated in time with a 4th order Runge-Kutta algorithm. At each substep, the spatial derivatives in the r.h.s. of the equations are evaluated using second order centered finite differences, except for the Poisson bracket terms evaluated with the Arakawa scheme.[35] The main subtlety appears in the parallel gradient. Although fields are discretized on a grid that uses the toroidal and straight-field-line coordinates, the parallel gradient is computed along the field line as described in Ref. 7

$$\nabla_\parallel A = qb_*^\theta R_0\left(\frac{\partial A}{\partial z} + \frac{a}{q}\frac{\partial A}{\partial y}\right) \equiv qb_*^\theta R_0 \frac{\partial A}{\partial \zeta}, \tag{52}$$

$$\frac{\partial A}{\partial \zeta} \equiv \frac{1}{2\Delta\zeta}(A_{i,j+\Delta j,k+1} - A_{i,j-\Delta j,k-1}), \tag{53}$$

where now the coefficient $qb^{\theta*}R_0$ contains ϵ corrections, $\zeta = z + ay/q$ is a field-following coordinate, $\Delta\zeta = \Delta z\sqrt{1 + \epsilon^2/\bar{q}^2}$, $\Delta j = N_y/(qN_z)$ and N_y (resp. N_z) are the number of grid points in the y (resp z) direction. In the present implementation Δj is constrained to be an integer. The second order parallel gradient is approximated as

$$\nabla_\parallel^2 A = (qb_*^\theta R_0)^2 \frac{\partial^2 A}{\partial \zeta^2}, \tag{54}$$

and the small term proportional to $\partial(qb^{\theta_*}R_0)/\partial\zeta$ has been neglected as it is usually extremely small.

After each substep of the fluid moments integration, the potential is obtained from the vorticity by solving the Poisson equation $\omega = \nabla_\perp^2\phi$, and boundary conditions described in Sec. II A are imposed. The 3D arrays are parallelized in the x and z direction using a standard message passing interface (MPI) domain decomposition. The Poisson solver is trivially parallelized in the z direction using the parallel (on the x communicator) direct solver MUMPS.[36]

Equations (9)–(14) can be expressed in (x,y,z) coordinates but further approximations on the Poisson bracket operator (see Appendix C) and on the perpendicular laplacian

(see Appendix A) allow to save significant central processing unit time.

Simulations are initialized with flat radial profiles and smooth poloidal profiles consistent with the boundary conditions described in Sec. II A. A small perturbation is then superimposed on top of them. After the simulation starts, the localized injection of density and temperature produces enough free energy to trigger a number of unstable modes that develop into turbulence. The simulations will therefore experience a transient phase followed by a quasi steady-state given by the interplay between the plasma sources, perpendicular transport, and parallel losses at the limiter plates. There is no separation between the background gradient and the fluctuations: the profile gradients are *a-priori* unknown and are extracted from the time-averaged data over the quasi steady-state.

GBS simulations have a fixed aspect ratio given by $\epsilon_{GBS} = 2\pi R_0/L_y$, where R_0 and $L_y = 2\pi a$ are specified in ρ_{s0} units on input. A fully consistent aspect ratio scan would imply to vary either R_0 (in other words the amplitude of the Poisson brackets) or L_y (in other words the plasma size $\rho^* = \rho_s/a$). In order to remain focused on the equilibrium effects only, the aspect ratio effects entering the various operators are handled with an aspect ratio parameter ϵ that is varied separately from the other parameters. Its value is then scanned from the "$s - \alpha$" value $\epsilon = 0$ to the realistic value $\epsilon = \epsilon_R = L_y/(2\pi R_0)$. Simulations for $\epsilon = 0, 1/8, 1/5, 1/4$ have been performed where the last value corresponds to the real aspect ratio. The other physical parameters are $q = 4$, $\hat{s} = 0$, $L_x = 100$, $L_y = 800$, $R_0 = 500$, $\nu = 0.1$, $m_i/m_e = 200$. The value of ν is consistent with typical values from experiments. The ion to electron mass ratio is smaller than the physical due to the Courant-Friedrichs-Lewy (CFL) constraint imposed by the explicit time integrator. This unphysical value could potentially affect the simulations results as it enhances the inertial branch of drift waves and ballooning modes. However, as the inertial branch becomes important if $\gamma m_i/m_e > \nu$,[28] in the considered parameter regime, the resistivity value is sufficiently high that one is far away from the resistive-inertial transition (see Ref. 11). Thus, the artificial high value of m_i/m_e does not influence the results. The source terms S_n and S_{T_e} in Eqs. (1) and (5) have a Gaussian shape centered at $x_S = 30$ with a characteristic width $\sigma_s = 5$ and have an amplitude of 1. The source profiles are flat in the y direction but decay exponentially at a distance of $40\rho_s$ from the top and bottom limiter. As these source terms mimic the outflow of plasma from the closed flux surface region, the simulations are physically meaningful for $x > x_S$. In a previous work,[10] the source strength was varied by a factor of four without significant changes in the dynamics. The shape of the source has been changed as well, without significantly impacting the results. The following numerical parameters were used for the simulations: $N_x = 128, N_y = 512, N_z = 64$, $\Delta t = 2 \cdot 10^{-4} R_0/c_s$. η_{0i} and η_{0e} have a fixed value of 4 in this work. η_{0i} is formally equal to 0 in a cold ion model, but a finite value is used for numerical stability; the value of η_{0e} used in GBS is usually larger than the physical one by 2 to 3 orders of magnitude. It has been checked that its influence on the simulation is very limited. $\chi_\parallel$ describes the amplitude of the parallel

diffusive heat flux. GBS simulations typically use $\chi_\parallel = 1$, much smaller than the Braginskii value. However, the simulations presented in this work are in the sheath-limited regime, where the parallel electron temperature gradient is small. The value of $\chi_\parallel$ has therefore little influence on the results and it has been checked that an increase of $\chi_\parallel$ by one order of magnitude does not modify the results. Finally, all the perpendicular diffusion coefficients have been set to 5. It is noted that reasonable values (of order unity) of the diffusion coefficients do not modify the results.

B. The gradient removal theory

In previous publications,[7,12] it has been demonstrated that the gradient removal turbulence saturation mechanism theory[10] leads to predictions of the SOL steady-state gradient in agreement with simulation results and experimental data.[37] The main features of this theory are briefly summarized here for completeness. The main hypothesis is that the linearly unstable modes saturate when the gradient associated with the perturbation equals the background one. This condition writes $\partial \delta p/\partial r \sim \partial p_0/\partial r$ and the turbulence saturation occurs when $\delta p/p_0 \sim \sigma_x/L_p$, where σ_x is the radial extension of the perturbation. Non-local linear theory[30,38] gives $\sigma_x \sim \sqrt{k_y/L_p}$. Then, using the leading order term in the pressure equation, i.e., $\partial p/\partial t \sim [\phi, p]$, the radial $E \times B$ flux can be expressed as $\Gamma \sim p_0\gamma/k_y$, where γ and k_y are, respectively, the growth rate and the poloidal wave number of the instability that dominates the transport. Finally, the nonlinear steady state can be written as a balance between the divergence of the perpendicular turbulent fluxes $\partial_r \Gamma_\perp \sim \Gamma/L_p$ and the parallel flux at the limiter plates $\nabla_\parallel \cdot \Gamma_\parallel \sim p_0 c_s/(qR_0)$ to obtain

$$\frac{L_p}{q} = \frac{R_0}{c_s}\left(\frac{\gamma}{k_y}\right)_{max}, \qquad (55)$$

within the hypotheses that $L_n \cong L_T$ and that turbulence is dominated by the mode that maximises the transport. This equation is a prediction of the pressure characteristic length in limited SOL plasmas and can be tested against numerical simulations. For this purpose, the values of $L_y, m_e/m_i, q, \epsilon$ and ν of the nonlinear simulations are used as input in the linear code to obtain the growth rate of the linear modes in the system. The value of η is extracted from the 4 different non-linear simulations, and a scan in (k_y, L_n) (assuming $k_y = k_Y$) is performed. For each L_n value, the k_y value that maximizes γ/k_y is used and Eq. (55) is solved for L_p.

C. Simulations results

Typical snapshots of the pressure profiles are displayed in Fig. 2. Turbulent eddies are produced at the source location and are transported radially outwards. The peak pressure increases with increasing ϵ while the value toward the right edge of the domain remains unchanged. The left panel of Fig. 3 shows the time evolution of the radial, poloidal, and toroidal average of R_0/L_p for the 4 different aspect ratios. The bursty behavior of turbulence is clearly seen on these curves. The standard deviation is roughly constant for all
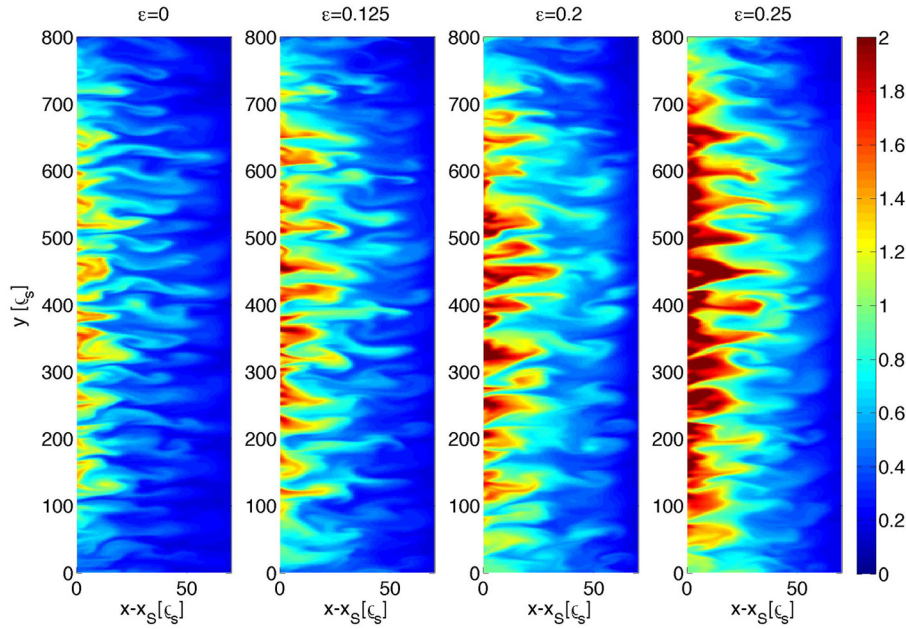
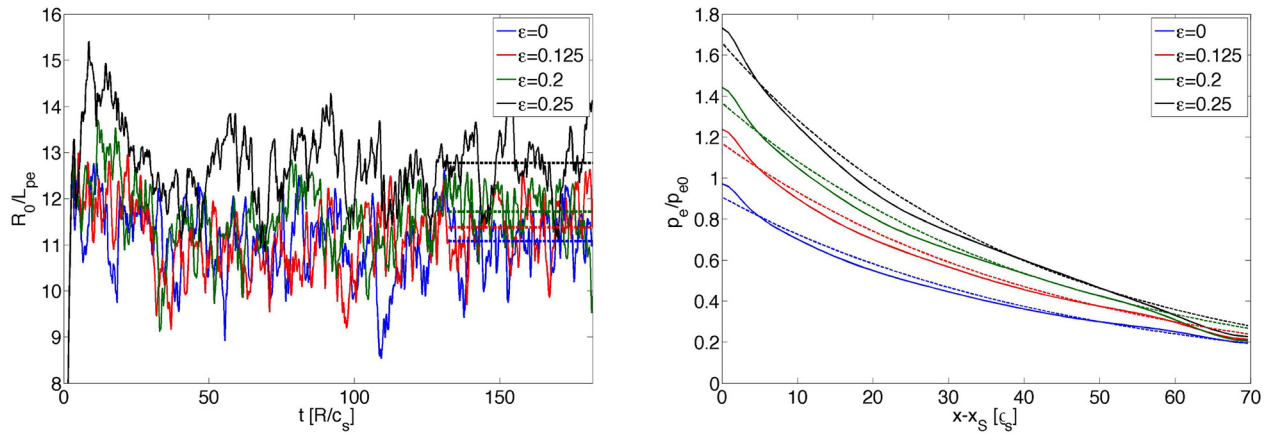FIG. 2. Poloidal snapshots of the pressure observed in the four different aspect ratio values.

FIG. 3. Left: time evolution of the normalized pressure gradient for simulations with different aspect ratios, averaged over the source free region. The dashed lines represent the average value over the last $50R_0/c_s$. Right: Radial profile pressure for simulations with different aspect ratios. The dashed lines are exponential fits of the form $\exp(-x/L_p)$, where L_p is the steady-state pressure characteristic length.

cases and is around 0.55. The time window to evaluate steady-state profile must be larger than the typical period of a burst and long enough to have a good statistic. For all cases, steady-state profiles are computed over a time window of 50 R_0/c_s, in a source free region of width $45\rho_s$ in x and containing the full domain in y and z. The steady-state value is $R_0/L_p = 11.2, 11.4, 11.7$, and 12.8 for $\epsilon = 0, 1/8, 1/5, 1/4$. In other words, decreasing the aspect ratio tends to increase the steady-state pressure gradient by 15% when going from the cylindrical to the realistic aspect ratio. The right panel of Fig. 3 shows the steady-state pressure radial profile and fits obtained with expressions of the form $p \sim \exp(-(x - x_S)/L_p)$. These fits describe well the numerical profiles.

The steady-state pressure gradient of these nonlinear simulations can be compared with the predictions of the gradient removal theory, Eq. (55) and are summarized in Table I. Good qualitative agreement is found for all simulation cases and the trend observed in nonlinear simulations is

recovered by the gradient removal theory. According to these results, the gradient removal theory predicts that as ϵ is increased, the gradient sustained inside the SOL increases. This change is due to the reduction of the growth rate as the poloidal wavelength of the mode maximizing γ/k_y is

TABLE I. Pressure gradients obtained from simulations and gradient removal theory. The gradients obtained from simulations are averaged poloidally, toroidally and radially between $x_1 = 35$ and $x_2 = 80$, and over a time window of $50R_0/c_s$ at the end of the simulation.

Simulation	$(R_0/L_p)_{\text{sim}}$	$(R_0/L_p)_{\text{GR}}$
$\epsilon = 0$	11.2	12.5
$\epsilon = 0.125$	11.4	13.1
$\epsilon = 0.2$	11.7	13.6
$\epsilon = 0.25$	12.8	14.1

unchanged by aspect ratio effects according to both the gradient removal theory and the nonlinear simulations.

In order to explain this result, the type of instability that dominates turbulent transport is characterized. A set of linear simulations using the density and temperature gradients obtained in nonlinear simulations have been performed in order to identify which is the dominant instability. To this aim, four simplified models[25] are used, in which either the resistivity or the electron inertia, and either the ballooning drive or the drift wave coupling have been neglected. These four models are limiting cases that describe the inertial drift wave, the inertial ballooning mode, the RDW, and the RBM. For each of these instabilities, a k_y scan is performed and it is supposed, in accordance with the gradient removal theory described above, that the instability with the maximum γ/k_y is the dominant one in nonlinear simulations. This procedure has been rigorously verified in a significant portion of the phase space $(q, m_e/m_i, \hat{s}, \nu)$[11] and is displayed in Fig. 4 for the $\epsilon = 0$ case. Clearly, the resistive ballooning mode is the dominant instability over the whole k_y spectrum, confirming previous findings.[11] The same result is obtained for the other ϵ scan values.

Another way to distinguish between drift waves and ballooning modes in nonlinear simulations is described in Ref. 39. Both types of instabilities occur in the presence of an $E \times B$ convection down a pressure gradient but the energy transfer channel is different. For drift waves, it is a (small) breaking of electron adiabaticity that allows a perturbation to grow, while, in the ballooning case, the energy transfers through the curvature operator. As a result, the phase shift between the potential and the pressure should be close to 0 for drift wave dominated turbulence, while it should be close to $\pi/2$ for ballooning-mode dominated turbulence.

Fig. 5 shows the probability distribution function (pdf) of the phase between the perturbed potential and the perturbed electron pressure as a function of k_y. The pdf is normalized to the pressure k_y spectrum amplitude such that the k_y modes that contribute most to the transport are enhanced. The plot shows that the phase is located around $\pi/3$. This

FIG. 5. pdf of the phase between the perturbed electrostatic potential and the perturbed electron pressure as a function of k_y. The pdf is normalized to the pressure k_y spectrum amplitude. The simulation is $\epsilon = 0.25$.

value, although not exactly equal to $\pi/2$, reflects a relatively pronounced ballooning character of the turbulence.

Having now established that the simulations are dominated by ballooning modes, one is now able to give an explanation to the increase of R_0/L_p when turning on aspect ratio effects. The linear dispersion relation described in Sec. IV predicts a stabilization of linear ballooning modes with increasing ϵ, while the k_y mode maximizing γ/k_y remains unchanged. Therefore, according to the gradient removal theory, the gradient sustained in nonlinear simulations increases with ϵ. This is indeed what is observed in GBS nonlinear simulations.

Fig. 6 shows the poloidal profile of $1/L_p$ normalised to its poloidal average. Beside a steepening of the average pressure gradients observed when finite aspect ratio effects are taken into account, one observes that the steepening is stronger on the part of the SOL above the equatorial midplane ($y > L_y/2 = 400$) than in the one below ($y < L_y/2 = 400$). This results from the $E \times B$ convection of a steeper profile
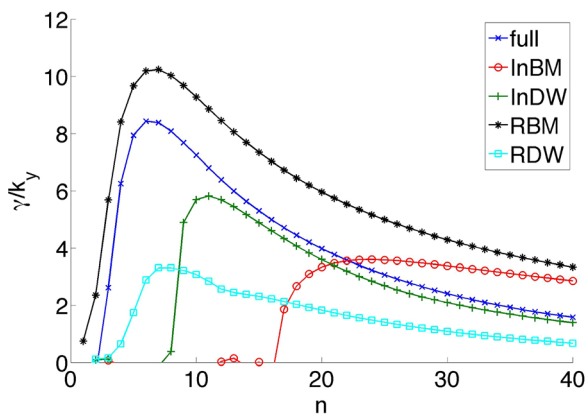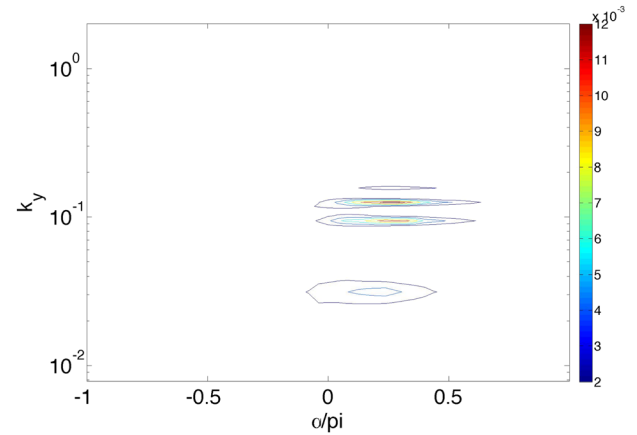

FIG. 4. Growth rate as a function of the toroidal mode number for reduced models describing the Inertial Ballooning Mode (InBM, red, circles), the Inertial Drift Wave (InDW, green, pluses), the RBM (black, stars), and the RDW (cyan, squares). The blue line with crosses shows the full model. Parameters are derived from the $\epsilon = 0$ GBS nonlinear simulations: $R_0/L_n = 6.6, \eta = 0.66, q = 4, \hat{s} = 0, \nu = 0.1, m_e/m_i = 1/200$.
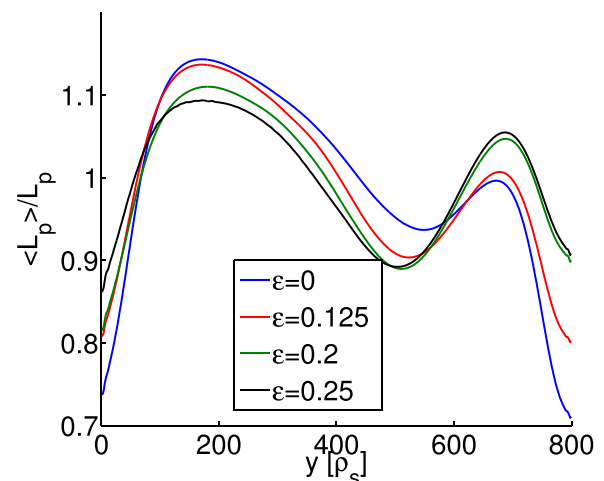

FIG. 6. Inverse characteristic pressure length in the poloidal direction, normalised to its poloidal average. The gradients obtained from simulations are averaged poloidally, toroidally, and radially between $x_1 = 35$ and $x_2 = 80$, and over a time window of $50R_0/c_s$ at the end of the simulation.

from the low-field side equatorial midplane to the $y > 0$ part of the SOL.

Aspect ratio effects do not seem to have any other measurable effect on the turbulence. An additional analysis reveals that the fluctuation level increases by approximately 2% when going from $\epsilon = 0$ to $\epsilon = 0.25$, and that the pdfs of the perturbations look extremely similar once normalised to the variance. The ballooning character and the radial correlation length are also similar between the different simulations. This similarity between the different simulations is explained by the relatively mild impact of aspect ratio effects on the equilibrium gradient.

VI. CONCLUSIONS

In the present work, the aspect ratio effects in circular geometry on SOL turbulence in a limiter configuration have been investigated. Results can be summarized as follows. First, the Braginskii equations have been extended to a general magnetic geometry, and the expression of the various differential operators has been given for an arbitrary set of coordinates. This constitutes a general framework to describe SOL turbulence in a more complex magnetic equilibrium in the future. In this work, one has focused on a circular flux surface configuration retaining aspect ratio effects. A linear analysis has revealed that aspect ratio effects stabilize pressure gradient driven modes. In more details, it is shown that the overall effect is mainly a balance between the destabilizing effects of the modified parallel gradient operator and the stabilizing effect of the $(1/B)$ C operator. This trend is recovered analytically by a simplified model describing ballooning modes. While the stabilization occurs for both RBM and RDW, the effect is more important on ballooning instabilities for which the curvature plays a major role. Then, the nonlinear simulations of SOL turbulence in limited configuration, carried out with the flux-driven fluid code GBS, confirm that the turbulence level is set according to the gradient removal theory. The pressure gradient, sustained in a nonlinear steady state by the interplay mechanism between a mimicked source from the core, turbulent perpendicular transport and parallel losses at the limiter sheaths, is related to the linear properties of the unstable modes present in the system. In this paper, the trend of GBS simulations is qualitatively reproduced by the gradient removal theory predictions, and it is shown that including aspect ratio effects increases the steady-state pressure gradient by 15%. This result is supported by a simple analytical dispersion relation describing the main features of ballooning modes, instability that is dominating transport for the phase space parameters considered. The other features of turbulence do not seem to be significantly affected by aspect ratio effects.

More generally, this work stresses the fact that finite aspect ratio effects on the SOL width in limited plasma seem to be well described by the gradient removal theory. This work therefore illustrates the fortunate situation where the impact of a change in one of the phase space parameter (for instance in the aspect ratio) on the SOL width does not affect the nature of the driving instability and therefore it can be qualitatively predicted using a simple dispersion relation. Future work will try to extend this result to a wider class of magnetic configurations, such as plasmas with Shafranov shift, elongation, and triangularity.

APPENDIX A: OPERATOR COEFFICIENTS IN GENERAL GEOMETRY

The coefficients derived in this section are computed from the contravariant and covariant metric in (r, α, θ_*) for the flux-tube geometry and in (θ_*, r, φ) for the toric geometry. In particular, $\mathcal{J} \equiv \mathcal{J}_{\theta_* r \varphi} = \mathcal{J}_{r\alpha\theta_*}$. The coefficients indexed with (XYZ) and (xyz) are obtained by renormalizing the partial derivatives. For example, $C(A) \propto \mathcal{C}^{\theta_*} \partial A/\partial\theta_* = a\mathcal{C}^{\theta_*} \partial A/\partial Y$. The coefficients in Eqs. (18) to (21) for the flux-tube geometry are given by

$$\mathcal{P}_{XY} = \frac{b_{\theta_*} a}{\mathcal{J} q}, \quad \mathcal{P}_{YZ} = \frac{a R_0 b_r}{\mathcal{J}}, \quad \mathcal{P}_{ZX} = \frac{q b_\alpha R_0}{\mathcal{J}}, \quad \text{(A1)}$$

$$\mathcal{D}^X = \mathcal{D}^Y = 0, \quad \mathcal{D}^Z = q R_0 b^{\theta_*}, \quad \text{(A2)}$$

$$\mathcal{C}^X = -\frac{B}{2\mathcal{J}} \frac{\partial c_\alpha}{\partial\theta_*}, \quad \mathcal{C}^Y = \frac{aB}{2\mathcal{J} q} \left(\frac{\partial c_r}{\partial\theta_*} - \frac{\partial c_{\theta_*}}{\partial r} \right),$$
$$\mathcal{C}^Z = \frac{q R_0 B}{2\mathcal{J}} \frac{\partial c_\alpha}{\partial r}, \quad \text{(A3)}$$

$$\mathcal{N}^{XX} = g^{rr}, \quad \mathcal{N}^{XY} = \frac{2g^{\alpha r} a}{q}, \quad \mathcal{N}^{YY} = \frac{a^2 g^{\alpha\alpha}}{q^2}, \quad \text{(A4)}$$

$$\mathcal{N}^X = \nabla^2 r, \quad \mathcal{N}^Y = \frac{a}{q} \nabla^2 \alpha,$$
$$\mathcal{N}^Z = q R_0 \left\{ \nabla^2 \theta_* - \frac{1}{\mathcal{J}} \frac{\partial}{\partial\theta_*} [\mathcal{J} (b^{\theta_*})^2] \right\}, \quad \text{(A5)}$$

$$\mathcal{N}^{ZZ} = q^2 R_0^2 (g^{\theta_* \theta_*} - (b^{\theta_*})^2), \quad \mathcal{N}^{XZ} = q R_0 g^{r\theta_*},$$
$$\mathcal{N}^{YZ} = R_0 a g^{\theta_* \alpha}, \quad \text{(A6)}$$

$$\nabla \cdot \mathbf{b} = \frac{1}{\mathcal{J}} \frac{\partial}{\partial\theta_*} (b^{\theta_*} \mathcal{J}), \quad \text{(A7)}$$

where $c_i = b_i/B$ and θ_* is defined by Eq. (24).

For the toric geometry (x,y,z), the perpendicular laplacian is approximated to lie in the poloidal plane to avoid a costly 3D solver. One has

$$\nabla_\perp^2 = \nabla_{pol}^2 - a^2 (b^{\theta_*})^2 \frac{\partial^2 A}{\partial y^2} - \frac{a}{\mathcal{J}} \frac{\partial}{\partial\theta_*} \left(\frac{\psi'^2}{\mathcal{J} B^2} \right) \frac{\partial A}{\partial y}$$
$$- 2a R_0 b^{\theta_*} b^\varphi \frac{\partial^2 A}{\partial y \partial z} + R_0^2 (b^{\theta_*})^2 \frac{\partial^2 A}{\partial z^2}, \quad \text{(A8)}$$

$$\nabla^2_{pol} = \frac{1}{\mathcal{J}} \frac{\partial}{\partial \xi^\mu} \left(\mathcal{J} g^{\mu\nu} \frac{\partial A}{\partial \xi^\nu} \right), \tag{A9}$$

where $\mu, \nu = \{\theta_*, r\}$. In Eq. (A8), terms after ∇^2_{pol} on the right hand side of (A8) are neglected. The second one is of order $\mathcal{O}(\epsilon^2)$ and the other ones are least ρ_{s0}/a times smaller than ∇^2_{pol}. The general coefficients are then given by

$$\mathcal{P}_{xy} = \frac{b_\varphi a}{\mathcal{J}}, \quad \mathcal{P}_{xz} = \frac{R_0 b_{\theta_*}}{\mathcal{J}}, \quad \mathcal{P}_{zx} = \frac{b_r a R_0}{\mathcal{J}}, \tag{A10}$$

$$\mathcal{D}^x = 0, \quad \mathcal{D}^y = ab^{\theta_*}, \quad \mathcal{D}^z = R_0 b^\varphi, \tag{A11}$$

$$\mathcal{C}^x = -\frac{B}{2\mathcal{J}} \frac{\partial c_\varphi}{\partial \theta_*}, \quad \mathcal{C}^y = \frac{aB}{2\mathcal{J}} \frac{\partial c_\varphi}{\partial r}, \quad \mathcal{C}^z = \frac{R_0 B}{2\mathcal{J}} \left(\frac{\partial c_r}{\partial \theta_*} - \frac{\partial c_{\theta_*}}{\partial r} \right), \tag{A12}$$

$$\mathcal{N}^{xx} = g^{rr}, \quad \mathcal{N}^{xy} = 2a g^{r\theta_*}, \quad \mathcal{N}^{yy} = a^2 g^{\theta_*\theta_*}, \tag{A13}$$

$$\mathcal{N}^x = \nabla^2 r, \quad \mathcal{N}^y = a \nabla^2 \theta_*, \tag{A14}$$

$$\nabla \cdot \mathbf{b} = \frac{1}{\mathcal{J}} \frac{\partial}{\partial \theta_*} (b^{\theta_*} \mathcal{J}). \tag{A15}$$

APPENDIX B: OPERATOR COEFFICIENTS FOR A CIRCULAR CONCENTRIC MAGNETIC CONFIGURATION WITH ASPECT RATIO EFFECTS

1. Flux-tube coordinate system

The general coefficients given in Eqs. (A1)–(A7) can be written specifically for the magnetic configuration described in Sec. III. The Poisson bracket coefficients are given by

$$\mathcal{P}_{XY} = \frac{\left(1 + \epsilon^2/\bar{q}^2\right)^{1/2}(1 - \epsilon \cos\theta_*)}{(1 - \epsilon^2)^{1/2}}, \tag{B1}$$

$$\mathcal{P}_{YZ} = \frac{1 - \epsilon \cos\theta_*}{\left(1 + \epsilon^2/\bar{q}^2\right)^{1/2}(1 - \epsilon^2)^{3/2}} \times \left[\hat{s}\theta_* q \frac{R_0}{a}(1 - \epsilon^2) + \frac{\epsilon^2 \sin\theta_*}{\bar{q}(1 - \epsilon^2)^{1/2}} \right], \tag{B2}$$

$$\mathcal{P}_{XZ} = \frac{q}{\left(1 + \epsilon^2/\bar{q}^2\right)^{1/2}} \frac{R_0}{a} \frac{1 - \epsilon \cos\theta_*}{(1 - \epsilon^2)^{1/2}}. \tag{B3}$$

The parallel gradient and $\nabla \cdot \mathbf{b}$ coefficients reads

$$\mathcal{D}^X = \mathcal{D}^Y = 0, \tag{B4}$$

$$\mathcal{D}^Z = \frac{1 - \epsilon \cos\theta_*}{\left(1 + \frac{\epsilon^2}{\bar{q}^2}\right)^{1/2}}, \tag{B5}$$

$$\nabla \cdot \mathbf{b} = -\frac{\epsilon \sin\theta_*}{\bar{q} R_0 h(\epsilon)(1 - \epsilon^2)^{3/2}}. \tag{B6}$$

The curvature operator coefficients are given by

$$\mathcal{C}^X = \frac{\sin\theta_*}{R_0 h(\epsilon)(1 - \epsilon^2)^{3/2}}, \tag{B7}$$

$$\mathcal{C}^Y = \frac{1}{h(\epsilon)(1 - \epsilon^2)^{3/2}} \frac{1}{R_0} \left\{ \left[-\cos\theta_* k(\epsilon) - \hat{s}\theta_* \sin\theta_* \right. \right.$$
$$\left. + k(\epsilon)p(\epsilon)(1 - \epsilon \cos\theta_*) - \frac{\epsilon^3 \sin\theta_*}{\bar{q}q(1 - \epsilon^2)^{3/2}} \right]$$
$$\left. + \frac{(1 - \epsilon \cos\theta_*)}{q} \left[\frac{\epsilon^2 \sin\theta_*}{\bar{q}(1 - \epsilon^2)^{3/2}} - qk'(\epsilon) \right] \right\}, \tag{B8}$$

$$\mathcal{C}^Z = -\frac{q}{a h(\epsilon)(1 - \epsilon^2)^{3/2}} [-\cos\theta_* + (1 - \epsilon \cos\theta_*)p(\epsilon)], \tag{B9}$$

where $h(\epsilon) = (1 + \epsilon^2/\bar{q}^2)^{1/2}/(1 - \epsilon^2), k(\epsilon) = h^2(\epsilon)(1 - \epsilon^2)^{3/2}, p(\epsilon) = h'(\epsilon)/h(\epsilon))$. The coefficients for the perpendicular laplacian are given by

$$\mathcal{N}^{XX} = 1, \tag{B10}$$

$$\mathcal{N}^{XY} = -2\hat{s}\theta_* + \frac{2\epsilon \sin\theta_*}{1 - \epsilon^2}, \tag{B11}$$

$$\mathcal{N}^{YY} = \frac{(1 - \epsilon \cos\theta_*)^2}{(1 - \epsilon^2)} + (\hat{s}\theta_*)^2 - 2\frac{\epsilon}{q}\hat{s}\theta_* \frac{\sin\theta_*}{1 - \epsilon^2} + \frac{\epsilon^2}{q^2} \left(\frac{1 - \epsilon \cos\theta_*}{1 - \epsilon^2} \right)^2, \tag{B12}$$

$$\mathcal{N}^X = \frac{1}{a} \frac{1}{1 - \epsilon^2} (1 + \epsilon \cos\theta_* - 2\epsilon^2), \tag{B13}$$

$$\mathcal{N}^Y = \frac{a}{q} \nabla^2\alpha \cong -\frac{1}{R_0} \frac{\sin\theta_*}{1 - \epsilon^2}, \tag{B14}$$

$$\mathcal{N}^{ZZ} = \frac{q^2 R_0^2}{r^2} \left[\frac{(1 - \epsilon \cos\theta_*)^2}{1 - \epsilon^2} + \frac{\epsilon^2 \sin^2\theta_*}{(1 - \epsilon^2)^2} - \frac{\epsilon^2}{\bar{q}^2} \frac{(1 - \epsilon \cos\theta_*)^2}{h^2(\epsilon)(1 - \epsilon^2)^3} \right], \tag{B15}$$

$$\mathcal{N}^Z = -\frac{q}{a} \frac{\sin\theta_*}{1 - \epsilon^2}, \tag{B16}$$

$$\mathcal{N}^{YZ} = q\hat{s}\theta_* \frac{\sin\theta_*}{1 - \epsilon^2} - q\frac{R_0}{a} \left(\frac{(1 - \epsilon \cos\theta_*)^2}{(1 - \epsilon^2)} + \frac{\epsilon^2 \sin^2\theta_*}{(1 - \epsilon^2)^2} \right), \tag{B17}$$

$$\mathcal{N}^{XZ} = -q\frac{\sin\theta_*}{1 - \epsilon^2}. \tag{B18}$$

2. Toric coordinate system

The general coefficients given in Eqs. (A10)–(A15) can be written specifically for the magnetic configuration described in Sec. III

$$\mathcal{P}_{xy} = \frac{1}{(1 + \epsilon^2/\bar{q}^2)^{1/2}} \frac{1 - \epsilon \cos\theta_*}{(1 - \epsilon^2)^{1/2}}, \tag{B19}$$

$$\mathcal{P}_{xz} = \frac{\epsilon(1 - \epsilon \cos\theta_*)}{\bar{q}(1 + \epsilon^2/\bar{q}^2)^{1/2}(1 - \epsilon^2)}, \tag{B20}$$

$$\mathcal{P}_{yz} = \epsilon^2 \bar{q} \frac{1 - \epsilon \cos \theta_*}{(1 + \epsilon^2/\bar{q}^2)^{1/2}(1 - \epsilon^2)^2}, \tag{B21}$$

$$\mathcal{D}^y = \frac{a}{R_0 q} \frac{1 - \epsilon \cos \theta_*}{(1 - \epsilon^2)(1 + \epsilon^2/\bar{q}^2)^{1/2}}, \tag{B22}$$

$$\mathcal{D}^z = \frac{q}{a} \mathcal{D}^y, \tag{B23}$$

$$\mathcal{C}^x = \frac{1}{R_0} \frac{\sin \theta_*}{(1 + \epsilon^2/\bar{q}^2)^{1/2}(1 - \epsilon^2)^{1/2}}, \tag{B24}$$

$$\mathcal{C}^y = \frac{1}{R_0} \frac{\cos \theta_* - (1 - \epsilon \cos \theta_*) p(\epsilon)}{(1 + \epsilon^2/\bar{q}^2)^{1/2}(1 - \epsilon^2)^{1/2}}, \tag{B25}$$

$$\mathcal{C}^z = \frac{1}{rh(\epsilon)(1 - \epsilon^2)^2 \bar{q}} \left[\frac{\epsilon^2}{2} \cos \theta_* - \frac{\epsilon^3}{2} \cos^2 \theta_* - \epsilon^3 \sin^2 \theta_* \right. $$
$$- \frac{g'(\epsilon)}{2}(1 - \epsilon^2)^{3/2}(1 - \epsilon \cos \theta_*)$$
$$\left. + \epsilon^2 (1 - \epsilon^2)(-\cos \theta_* + (1 - \epsilon \cos \theta_*) p(\epsilon)) \right], \tag{B26}$$

$$\mathcal{N}^{xx} = 1, \tag{B27}$$

$$\mathcal{N}^{xy} = -2\epsilon \frac{\sin \theta_*}{1 - \epsilon^2}, \tag{B28}$$

$$\mathcal{N}^{yy} = \frac{a^2}{r^2} \left(\frac{(1 - \epsilon \cos \theta_*)^2}{1 - \epsilon^2} + \frac{\epsilon^2 \sin^2 \theta_*}{(1 - \epsilon^2)^2} \right), \tag{B29}$$

$$\mathcal{N}^x = \frac{1}{a} \frac{1}{1 - \epsilon^2} (1 + \epsilon \cos \theta_* - 2\epsilon^2), \tag{B30}$$

$$\mathcal{N}^y = -\frac{1}{R_0} \frac{\sin \theta_*}{(1 - \epsilon^2)^2}, \tag{B31}$$

where $g(\epsilon) = \epsilon^2/\bar{q}/\sqrt{1 - \epsilon^2}$. The toric geometry differs from the flux-tube one in the fact that local magnetic shear effects are not included in the metric tensor. In flux-tube geometry, shear effects are directly present when computing $\nabla \alpha = \nabla(\varphi - q(r)\theta_*)$. In global geometry, shear effects are introduced by applying the following transformation:

$$\hat{\theta}_* = \theta_* + \hat{s}\theta_* \frac{r - a}{a}, \tag{B32}$$

where it is assumed that $\Delta_{\mathrm{SOL}} \ll a$ where $\Delta_{SOL} \sim r - a$ is the SOL width. The main modifications are given by

$$g^{r\hat{\theta}_*} = g^{r\theta_*} + \frac{\hat{s}\theta_*}{a} g^{rr}, \tag{B33}$$

$$g^{\hat{\theta}_*\hat{\theta}_*} = g^{\theta_*\theta_*} + 2\frac{\hat{s}\theta_*}{a} g^{r\theta_*} + \frac{(\hat{s}\theta_*)^2}{a^2} g^{rr}, \tag{B34}$$

$$\left. \frac{\partial}{\partial r} \right)_{\hat{\theta}_*} A(r, \theta_*(r, \hat{\theta}_*)) = \left. \frac{\partial A}{\partial r} \right)_{\theta_*} + \frac{\partial A}{\partial \theta_*} \left. \frac{\partial \theta_*}{\partial r} \right)_{\hat{\theta}_*}. \tag{B35}$$

APPENDIX C: THE $\epsilon \to 0$ LIMIT

The coefficients described in Appendix B can be simply computed in the $\epsilon \to 0$ limit. For the purpose of this analysis, the flux-tube coordinate system is considered. Similar results are obtained when using the toric coordinate system

$$\lim_{\epsilon \to 0} \mathcal{P}_{XY} = 1, \tag{C1}$$

$$\lim_{\epsilon \to 0} \mathcal{P}_{YZ} = \hat{s}\theta_* q \frac{R_0}{a}, \tag{C2}$$

$$\lim_{\epsilon \to 0} \mathcal{P}_{XZ} = q \frac{R_0}{a}. \tag{C3}$$

Approximating $\partial_X \to k_X$, $\partial_Y \to k_Y$, $\partial_Z \to k_Z$, one finds

$$\left| \frac{\mathcal{P}_{XZ}[\phi, A]_{XZ}}{\mathcal{P}_{YX}[\phi, A]_{YX}} \right| \sim q \frac{R_0}{a} \frac{k_Z}{k_Y} \sim \mathcal{O}(1/(k_Y a)), \tag{C4}$$

$$\left| \frac{\mathcal{P}_{ZY}[\phi, A]_{ZY}}{\mathcal{P}_{YX}[\phi, A]_{YX}} \right| \sim \mathcal{O}(1/(k_X a)). \tag{C5}$$

Assuming that typical turbulence structure have $k_X \sim \sqrt{k_Y/L_p}$,[38] $k_Z \sim 1/(qR)$, $k_Y \sim 0.1/\rho_{s0}$, $R_0/L_p \sim 10^1 - 10^2$, the terms containing $\mathcal{P}_{YZ}$ and $\mathcal{P}_{XZ}$ can be neglected. The same kind of argument is used to neglect $\mathcal{P}_{yz}$ and $\mathcal{P}_{xz}$ in toric geometry.

As $\lim_{\epsilon \to 0} \mathcal{D}^Z = 1$ the parallel gradient simply becomes $\nabla_\parallel = \partial/\partial Z$ and $\lim_{\epsilon \to 0} \nabla \cdot \mathbf{b} = 0$ therefore related terms can be neglected.

The curvature operator coefficients are given by

$$\lim_{\epsilon \to 0} \mathcal{C}^X = \frac{\sin \theta_*}{R_0}, \tag{C6}$$

$$\lim_{\epsilon \to 0} \mathcal{C}^Y = \frac{-\cos \theta_* - \hat{s}\theta_* \sin \theta_*}{R_0}, \tag{C7}$$

$$\lim_{\epsilon \to 0} \mathcal{C}^Z = \frac{q \cos \theta_*}{a}, \tag{C8}$$

and one sees that $\mathcal{C}^Z$ in normalized units is a/ρ_s times smaller than unity and can be therefore neglected. Finally, the coefficients for the laplacian are given by:

$$\lim_{\epsilon \to 0} \mathcal{N}^{XX} = 1, \tag{C9}$$

$$\lim_{\epsilon \to 0} \mathcal{N}^{XY} = -2\hat{s}\theta_*, \tag{C10}$$

$$\lim_{\epsilon \to 0} \mathcal{N}^{YY} = 1 + (\hat{s}\theta_*)^2, \tag{C11}$$

$$\lim_{\epsilon \to 0} \mathcal{N}^X = \frac{1}{a}, \tag{C12}$$

$$\lim_{\epsilon \to 0} \mathcal{N}^Y = -\frac{1}{R_0}. \tag{C13}$$

Like for the $\mathcal{C}^Z$ coefficient, $\mathcal{N}^X$ and $\mathcal{N}^Y$ are extremely small and are usually neglected

$$\lim_{\epsilon \to 0} \mathcal{N}^{ZZ} = \frac{q^2 R_0^2}{a^2}, \tag{C14}$$

$$\lim_{\epsilon \to 0} \mathcal{N}^Z = -\frac{q}{a} \sin \theta_*, \tag{C15}$$

$$\lim_{\epsilon \to 0} \mathcal{N}^{YZ} = q\hat{s}\theta_* \sin\theta_* - q\frac{R_0}{a}, \qquad (C16)$$

$$\lim_{\epsilon \to 0} \mathcal{N}^{XZ} = -q \sin\theta_*. \qquad (C17)$$

Those terms will all be small as they are multiplied by derivatives in the Z direction giving a $(1/R_0) \ll 1$ factor. These expressions describe the $s - \alpha$ model without Shafranov shift. Note that earlier implementations of the $s - \alpha$ model in gyro kinetic codes have been found inconsistent,[22] leading to significant differences on the growth rate of ion-temperature-gradient turbulence in the core. The reason was that trapping effects of order ϵ were retained in the modulus of the magnetic field only. At the plasma edge, trapping is usually neglected due to the high collisionality and no ϵ effects are retained. Therefore, the ordering $s - \alpha$ implementation in GBS is done in a consistent way.

[1]B. D. Dudson, M. V. Umansky, X. Q. Xu, P. B. Snyder, and H. R. Wilson, Comput. Phys. Commun. **180**, 1467 (2009).

[2]V. Naulin, Phys. Plasmas **10**, 4016 (2003).

[3]A. Zeiler, D. Biskamp, J. F. Drake, and P. N. Guzdar, Phys. Plasmas **3**, 2951 (1996).

[4]B. D. Scott, Plasma Phys. Controlled Fusion **48**, B277 (2006).

[5]T. Ribeiro, Plasma Phys. Controlled Fusion **47**, 1657 (2005).

[6]Y. Sarazin and P. Ghendrih, Phys. Plasmas **5**, 4214 (1998).

[7]P. Ricci, F. D. Halpern, S. Jolliet, J. Loizu, A. Mosetto, A. Fasoli, I. Furno, and C. Theiler, Plasma Phys. Controlled Fusion **54**, 124047 (2012).

[8]F. Militello, W. Fundamenski, V. Naulin, and A. H. Nielsen, Plasma Phys. Controlled Fusion **54**, 095011 (2012).

[9]P. Tamain, P. Ghendrih, E. Tsitrone, V. Grandgirard, X. Garbet, Y. Sarazin, E. Serre, G. Ciraolo, and G. Chiavassa, J. Comput. Phys. **229**, 361 (2010).

[10]P. Ricci and B. N. Rogers, Phys. Plasmas **20**, 010702 (2013).

[11]A. Mosetto, F. D. Halpern, S. Jolliet, J. Loizu, and P. Ricci, Phys. Plasmas **20**, 092308 (2013).

[12]F. D. Halpern, S. Jolliet, J. Loizu, A. Mosetto, and P. Ricci, Phys. Plasmas **20**, 052306 (2013).

[13]G. Rewoldt, W. M. Tang, and M. S. Chance, Phys. Fluids **25**, 480 (1982).

[14]A. Kirk, W. Fundamenski, J.-W. Ahn, and G. Counsell, Plasma Phys. Controlled Fusion **45**, 1445 (2003).

[15]N. R. Walkden, B. D. Dudson, and G. Fishpool, Plasma Phys. Controlled Fusion **55**, 105005 (2013).

[16]T. Takizuka, K. Shimizu, N. Hayashi, M. Hosokawa, and M. Yagi, Nucl. Fusion **49**, 075038 (2009).

[17]P. J. Harbour, Nucl. Fusion **35**, 759 (1995).

[18]A. Kendl and B. D. Scott, Phys. Plasmas **13**, 012504 (2006).

[19]B. D. Scott, Plasma Phys. Controlled Fusion **39**, 471 (1997).

[20]P. Angelino, X. Garbet, L. Villard, A. Bottino, S. Jolliet, P. Gendrih, V. Grandgirard, B. F. McMillan, Y. Sarazin, G. Dif-Pradalier, and T. M. Tran, Phys. Plasmas **15**, 062306 (2008).

[21]J. R. Robinson, B. Hnat, A. Thyagaraja, K. G. McClements, P. J. Knight, and A. Kirk, Phys. Plasmas **20**, 052302 (2013).

[22]X. Lapillonne, S. Brunner, T. Dannert, S. Jolliet, A. Marinoni, L. Villard, T. Goerler, F. Jenko, and F. Merz, Phys. Plasmas **16**, 032308 (2009).

[23]J. Loizu, P. Ricci, F. D. Halpern, and S. Jolliet, Phys. Plasmas **19**, 122307 (2012).

[24]F. Hariri and M. Ottaviani, Comput. Phys. Commun. **184**, 2419 (2013).

[25]A. Mosetto, F. D. Halpern, S. Jolliet, and P. Ricci, Phys. Plasmas **19**, 112103 (2012).

[26]J. W. Connor, R. J. Hastie, and J. B. Taylor, Phys. Rev. Lett. **40**, 396 (1978).

[27]P. N. Guzdar, J. F. Drake, D. McCarthy, A. B. Hassam, and C. S. Liu, Phys. Fluids B **5**, 3712 (1993).

[28]P. Ricci and B. N. Rogers, Phys. Plasmas **16**, 092307 (2009).

[29]P. Ricci and B. N. Rogers, Phys. Rev. Lett. **104**, 145001 (2010).

[30]P. Ricci, B. N. Rogers, and S. Brunner, Phys. Rev. Lett. **100**, 225002 (2008).

[31]B. Li, B. N. Rogers, P. Ricci, K. W. Gentle, and A. Bhattacharjee, Phys. Rev. E **83**, 056406 (2011).

[32]A. Fasoli, B. Labit, M. McGrath, S. H. Müller, and G. Plyushchev, Phys. Plasmas **13**, 055902 (2006).

[33]P. Ricci, C. Theiler, A. Fasoli, I. Furno, and B. Labit, Phys. Plasmas **16**, 055703 (2009).

[34]P. Ricci, C. Theiler, A. Fasoli, I. Furno, K. Gustafson *et al.*, Phys. Plasmas **18**, 032109 (2011).

[35]A. Arakawa, J. Comput. Phys. **1**, 119 (1966).

[36]P. R. Amestoy, I. S. Duffand, and J.-Y. L'Excellent, Comput. Methods Appl. Mech. Eng. **184**, 501 (2000).

[37]F. D. Halpern, P. Ricci, B. Labit, I. Furno, S. Jolliet, J. Loizu, A. Mosetto, G. Arnoux, J. P. Gunn, J. Horacek, M. Kocan, B. LaBombard, C. Silva, and J. E. Contributors, Nucl. Fusion **53**, 122001 (2013).

[38]B. N. Rogers and W. Dorland, Phys. Plasmas **12**, 062511 (2005).

[39]B. D. Scott, Phys. Plasmas **12**, 102307 (2005).